

Optimal control of coherent light scattering for binary decision problems

Supplementary information

Dorian Bouchet,¹ Lukas M. Rachbauer,² Stefan Rotter,² Allard P. Mosk,³ and Emmanuel Bossy¹

¹*Université Grenoble Alpes, CNRS, LIPhy, 38000 Grenoble, France*

²*Institute for Theoretical Physics, Vienna University of Technology (TU Wien), Vienna, Austria*

³*Nanophotonics, Debye Institute for Nanomaterials Science and Center for Extreme Matter and Emergent Phenomena, Utrecht University, P.O. Box 80000, 3508 TA Utrecht, Netherlands*

S1. OPTIMAL INCIDENT STATE

S1.1. General case

We define the incident field state $|E^{\text{in}}\rangle$ in the Hilbert space of all incident spatial modes. This state is characterized by the coefficients $\{E_1^{\text{in}}, \dots, E_M^{\text{in}}\}$, defined as the expectation values of the field operator in M incoming spatial modes. After interacting with a scattering system, such an incident state produces an outgoing field state $|E_i^{\text{out}}\rangle$, defined in the Hilbert space of all outgoing spatial modes, and where i denotes the configuration of the scattering system interacting with the field ($i = 1$ if H_1 is true, and $i = 2$ if H_2 is true). Outgoing field states are characterized by the coefficients $\{E_{i,1}^{\text{out}}, \dots, E_{i,N}^{\text{out}}\}$, defined as the expectation values of the field operator in N outgoing spatial modes. As a convention, we express the fields in units of $\sqrt{(2\hbar\omega)/(\epsilon_0 c_0 \Delta t A)}$, where \hbar is the reduced Planck constant, ω is the angular frequency of the field, ϵ_0 is the vacuum permittivity, c_0 is the speed of light in vacuum, Δt is the integration time and A is the effective mode area [1]. In this way, the average numbers of photons in the incident and outgoing states are expressed by $\langle E^{\text{in}}|E^{\text{in}}\rangle$ and $\langle E^{\text{out}}|E^{\text{out}}\rangle$, respectively. Using a scattering matrix formalism, incident and outgoing field states are related by the following expression:

$$|E_i^{\text{out}}\rangle = S_i |E^{\text{in}}\rangle, \quad (\text{S1})$$

where S_i is the scattering matrix associated with the i -th hypothesis. In order to separately study the role of the total number of photons $n = \langle E^{\text{in}}|E^{\text{in}}\rangle$ in the incident state and that of its spatial distribution, we define the normalized incident state $|\mathcal{E}^{\text{in}}\rangle = n^{-1/2}|E^{\text{in}}\rangle$ so that $\langle \mathcal{E}^{\text{in}}|\mathcal{E}^{\text{in}}\rangle = 1$. Writing $E_{i,k}^{\text{out}}$ as a projection of $|E_i^{\text{out}}\rangle$ on the state $|k\rangle$ associated with the k -th spatial mode, we obtain

$$E_{i,k}^{\text{out}} = \sqrt{n} \langle k|S_i|\mathcal{E}^{\text{in}}\rangle. \quad (\text{S2})$$

The statistical distance d_{12} is defined as follows:

$$d_{12}^2 = \frac{1}{n} \sum_{k=1}^N |E_{2,k}^{\text{out}} - E_{1,k}^{\text{out}}|^2. \quad (\text{S3})$$

Inserting Eq. (S2) into Eq. (S3) yields

$$d_{12}^2 = \sum_{k=1}^N |\langle k|S_2 - S_1|\mathcal{E}^{\text{in}}\rangle|^2. \quad (\text{S4})$$

This expression can be expanded into

$$d_{12}^2 = \sum_{k=1}^N \langle \mathcal{E}^{\text{in}}|(S_2 - S_1)^\dagger |k\rangle \langle k|S_2 - S_1|\mathcal{E}^{\text{in}}\rangle. \quad (\text{S5})$$

Using the completeness relation $\sum_k |k\rangle \langle k| = I_N$ where I_N is the N -dimensional identity matrix, we finally obtain

$$d_{12}^2 = \langle \mathcal{E}^{\text{in}}|D_{12}|\mathcal{E}^{\text{in}}\rangle, \quad (\text{S6})$$

where we introduced the discrimination operator

$$D_{12} = (S_2 - S_1)^\dagger (S_2 - S_1). \quad (\text{S7})$$

This operator, which is Hermitian by construction, quantifies the statistical distance between two scattering matrices. Its largest eigenvalue is equal to the maximum value of d_{12}^2 that can be reached by shaping the incident field state in its spatial degrees of freedom, and the eigenvector associated with this eigenvalue gives the spatial distribution of this optimal incident field state.

S1.2. Unitary limit

For two scattering matrices that are unitary ($S_i^\dagger = S_i^{-1}$), the operator D_{12} is expressed by

$$D_{12} = 2I_N - 2\text{Re}(S_2^\dagger S_1), \quad (\text{S8})$$

where $\text{Re}(S_2^\dagger S_1)$ denotes the Hermitian part of $S_2^\dagger S_1$. In this case, the eigenstates of D_{12} satisfy the eigenvalue equation:

$$(S_2^\dagger S_1 + S_1^\dagger S_2)|\mathcal{E}^{\text{in}}\rangle = (2 - \Lambda)|\mathcal{E}^{\text{in}}\rangle, \quad (\text{S9})$$

where $\Lambda \in \mathbb{R}$ denotes an eigenvalue of D_{12} . This equation can be identified as the eigenvalue equation for scattering invariant modes [2]. Since both S_1 and S_2 are unitary, the eigenstates of D_{12} satisfy the following generalized eigenvalue equation:

$$S_2|\mathcal{E}^{\text{in}}\rangle = e^{i\theta} S_1|\mathcal{E}^{\text{in}}\rangle, \quad (\text{S10})$$

where $\theta \in \mathbb{R}$. Thus, when eigenstates of D_{12} propagate into each scattering system, the resulting outgoing field states satisfy $|E_2^{\text{out}}\rangle = e^{i\theta}|E_1^{\text{out}}\rangle$, which shows that both outgoing fields are identical except for a phase change of θ . This phase change is related to the eigenvalue Λ by the following relation:

$$\Lambda = 2(1 - \cos \theta). \quad (\text{S11})$$

The statistical distance d_{12} is minimum when $\theta = 2\pi m$, $m \in \mathbb{Z}$; in such case, $d_{12}^2 = 0$ and the phase of the outgoing state does not depend on the scattering system the wave propagates in. In contrast, the statistical distance d_{12} is maximum when $\theta = \pi + 2\pi m$, $m \in \mathbb{Z}$; in such case, $d_{12}^2 = 4$ due to a phase difference of π in the outgoing state when the scattering system is changed.

S2. RATE OF ERROR FOR THE HOMODYNE SCHEME

S2.1. Noise statistics

In the experiment, we implemented a homodyne scheme based on digital off-axis holography. In the shot-noise limit and with a strong reference beam ($|E_k^{\text{ref}}|^2 \gg |E_{i,k}^{\text{out}}|^2$), the complex field retrieved by such homodyne scheme can be modeled by an N -dimensional complex random variable Z such that [3]

$$\text{Re } Z_k \sim \mathcal{N}(\text{Re } E_{1,k}^{\text{out}}, \sigma^2) \text{ and } \text{Im } Z_k \sim \mathcal{N}(\text{Im } E_{1,k}^{\text{out}}, \sigma^2) \text{ if } H_1 \text{ is true,} \quad (\text{S12a})$$

$$\text{Re } Z_k \sim \mathcal{N}(\text{Re } E_{2,k}^{\text{out}}, \sigma^2) \text{ and } \text{Im } Z_k \sim \mathcal{N}(\text{Im } E_{2,k}^{\text{out}}, \sigma^2) \text{ if } H_2 \text{ is true,} \quad (\text{S12b})$$

where $\sigma^2 = 1/2$. In practice, for measured data to follow these statistics, it is required to determine the value of the internal gain of the camera, which is approximately 8.8 photo-electrons per digital count for our camera (Basler acA1300-200um). Multiplying measured images by this gain factor ensures that intensities are expressed in terms of numbers of photons—the sub-unitary quantum efficiency of the camera being then implicitly included in the definition of measured transmission matrices.

To demonstrate that the data measured with our setup follow these statistics, we considered a data set composed of 4000 fields measured in low-light conditions. Among them, 2000 fields were measured in the presence of the target,

and 2000 fields were measured without the target. After subtracting the mean fields associated with the two different scattering systems, we calculated the variance of field quadratures for each outgoing mode (Fig. S1a). It clearly appears that the measured variance is uniform, and that its value is in excellent agreement with the theoretical value $\sigma^2 = 1/2$. Taking into account all modes within the field of view, we also verified that the measured distribution of the field quadratures is a centered normal distribution (Fig. S1b). Results presented here were obtained with the optimal incident state, a target composed of a single bead, and $n = 2.9 \times 10^5$ incident photons. Nevertheless, similar results were obtained for all data presented in Fig. 3 of the manuscript, that were all acquired in low-light conditions.

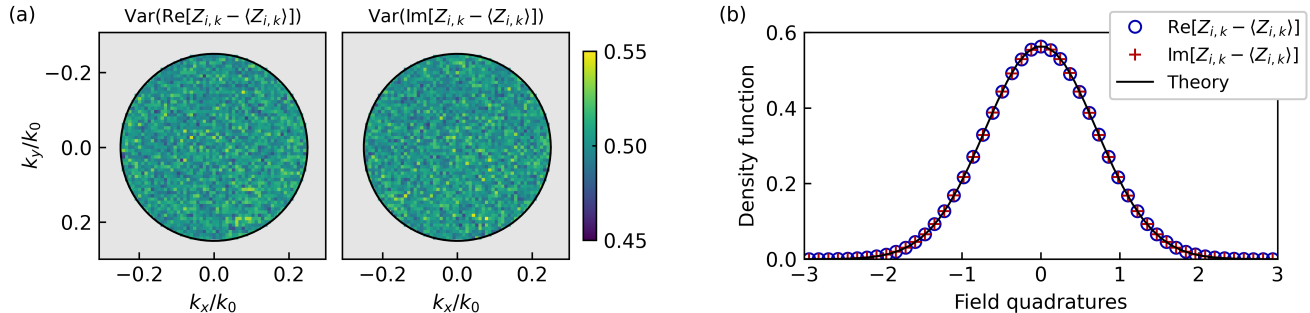


FIG. S1. (a) Variance of the real part and the imaginary part of the field, experimentally measured with a homodyne scheme in an off-axis configuration. k_0 denotes the norm of the wavevector, while k_x and k_y denote its components along the x and y directions, respectively. (b) Measured distributions of the field quadratures, after subtraction of the mean fields. The theoretical distribution is a centered normal distribution of variance $\sigma^2 = 1/2$. All figures are obtained from $N_{\text{rep}} = 4000$ measured fields composed of $N = 2617$ spatial modes. These fields were acquired using the optimal incident state and $n = 2.9 \times 10^5$ incident photons.

S2.2. Theoretical probability of error

The minimum probability of error that can be achieved when choosing a hypothesis from measured data is expressed by [4]

$$P_G = \frac{\pi_1}{2} \operatorname{erfc} \left[\sqrt{\frac{nd_{12}^2}{8\sigma^2}} + \ln \left(\frac{\pi_1}{\pi_2} \right) \sqrt{\frac{\sigma^2}{2nd_{12}^2}} \right] + \frac{\pi_2}{2} \operatorname{erfc} \left[\sqrt{\frac{nd_{12}^2}{8\sigma^2}} - \ln \left(\frac{\pi_1}{\pi_2} \right) \sqrt{\frac{\sigma^2}{2nd_{12}^2}} \right], \quad (\text{S13})$$

where π_1 and π_2 are the *a priori* probabilities associated with each hypothesis. Assuming that $\pi_1 = \pi_2 = 0.5$, we obtain

$$P_G = \frac{1}{2} \operatorname{erfc} \left(\sqrt{\frac{nd_{12}^2}{8\sigma^2}} \right). \quad (\text{S14})$$

When estimating the probability of error P_G from a finite number of trials N_{rep} , the number of errors that are observed follows a binomial distribution. The variance of the estimate \hat{P}_G is then given by

$$\operatorname{Var}(\hat{P}_G) = \frac{P_G(1 - P_G)}{N_{\text{rep}}}. \quad (\text{S15})$$

For N_{rep} sufficiently large, the probability distribution of \hat{P}_G approaches a normal distribution. This property allows us to define the following 95,4% confidence interval:

$$\left[P_G - 2\sqrt{\frac{P_G(1 - P_G)}{N_{\text{rep}}}}; P_G + 2\sqrt{\frac{P_G(1 - P_G)}{N_{\text{rep}}}} \right]. \quad (\text{S16})$$

S2.3. Measured rate of error

The rate of error observed in the experiment is obtained by processing noisy data Z using the likelihood-ratio test, which theoretically reaches the bound expressed by Eq. (S13). The decision criterion is given by

$$\ln l(Z) < \ln \left(\frac{\pi_1}{\pi_2} \right) \rightarrow \text{choose } H_1, \quad (\text{S17a})$$

$$\ln l(Z) > \ln \left(\frac{\pi_1}{\pi_2} \right) \rightarrow \text{choose } H_2, \quad (\text{S17b})$$

$$\ln l(Z) = \ln \left(\frac{\pi_1}{\pi_2} \right) \rightarrow \text{choose either } H_1 \text{ or } H_2, \quad (\text{S17c})$$

where $\ln l(Z)$ is the log-likelihood ratio expressed by [4]

$$\ln l(Z) = \text{Re} \left[\sum_{k=1}^N \frac{(E_{2,k}^{\text{out}} - E_{1,k}^{\text{out}})^* Z_k}{\sigma^2} \right] + \sum_{k=1}^N \frac{|E_{1,k}^{\text{out}}|^2 - |E_{2,k}^{\text{out}}|^2}{2\sigma^2}. \quad (\text{S18})$$

Calculating the log-likelihood ratio requires the knowledge of $E_{1,k}^{\text{out}}$ and $E_{2,k}^{\text{out}}$, which are the expectation values of the field under each hypothesis and for each outgoing spatial mode. These fields can be expressed as follows:

$$E_{1,k}^{\text{out}} = \frac{E_{s,k}^{\text{out}} - E_{d,k}^{\text{out}}}{2\pi_1}, \quad (\text{S19a})$$

$$E_{2,k}^{\text{out}} = \frac{E_{s,k}^{\text{out}} + E_{d,k}^{\text{out}}}{2\pi_2}, \quad (\text{S19b})$$

where we introduced $E_{s,k}^{\text{out}} = \pi_1 E_{1,k}^{\text{out}} + \pi_2 E_{2,k}^{\text{out}}$ and $E_{d,k}^{\text{out}} = \pi_2 E_{2,k}^{\text{out}} - \pi_1 E_{1,k}^{\text{out}}$. There are different possible strategies to assess $E_{s,k}^{\text{out}}$ and $E_{d,k}^{\text{out}}$. A straightforward strategy entails estimating both $E_{s,k}^{\text{out}}$ and $E_{d,k}^{\text{out}}$ from measurements performed with a large number of incident photons. Here, we opted for a different strategy, in which $E_{d,k}^{\text{out}}$ is estimated from measurements performed with a large number of incident photons, but with $E_{s,k}^{\text{out}}$ being directly assessed from the data measured in low-light conditions by averaging them over noise fluctuations ($E_{s,k}^{\text{out}} \simeq \langle Z_k \rangle$). This strategy, which is relevant only when N_{rep} is sufficiently large, allows to reduce biases that are observed when processing experimental data, including those due to unwanted reflections of the reference field by the camera sensor, to wavefront distortions generated by the optical elements used to control the incident photon flux, and to power fluctuations of the incident laser beam. Nevertheless, biases can also appear in this case due to the finite number of measurements used to estimate $E_{s,k}^{\text{out}}$, resulting in an observed rate of error that is slightly higher than the theoretically-predicted one (see Fig. 3 of the manuscript).

S3. EXPERIMENTAL IMPLEMENTATION

S3.1. Optical setup

The optical setup used to acquire transmission matrices and perform measurements in low-light conditions is represented in Fig. S2. The sample under study is composed of polystyrene beads dispersed on a glass coverslip. To prepare this sample, we used a commercial solution of polystyrene beads (Polysciences Polybead, diameter $3 \mu\text{m} \pm 150 \text{nm}$) that we diluted into 99% isopropyl alcohol. We then deposited it onto a clean glass coverslip and let it dry; this results in a sample with a very low density of beads (approximately 1 bead inside a $100 \mu\text{m} \times 100 \mu\text{m}$ area). Using this procedure, some of these beads are isolated, while others are aggregated into clusters. This allows us to study both the case of one isolated bead, and the case of a cluster of beads.

The light source used in our experiments is a continuous-wave solid-state laser (Cobolt 08-DPL) emitting at $\lambda = 532 \text{nm}$. The laser light is coupled to a single-mode polarization-maintaining fiber and out-coupled using a collimator (Schäfter+Kirchhoff 60FC-L-4-M75-01). A linear polarizer is used to ensure that the light is linearly polarized. The beam is separated into a signal path and a reference path using a 90:10 (transmission:reflection) beamsplitter.

In the signal path, the light beam passes through a variable attenuator composed of a neutral density filter of fractional transmittance $\mathcal{T}_{\text{nd}} = 10^{-3.6}$ mounted on a motorized flip mount (Thorlabs MFF101/M), a half wave-plate

mounted on a motorized rotation mount (Thorlabs PRM1/MZ8) and a linear polarizer. The light beam is reflected and modulated with a DMD (Vialux superspeed V-7001) using Lee holography [5], at a rate of 1400 Hz. Light passes through a 4f system composed of a 200 mm lens (L1) and 30 mm lens (L2). An iris located in the focal plane in-between the two lenses selects the first diffraction order of the grating displayed by the DMD.

A first scattering layer composed of one ground glass diffuser (Thorlabs DG20-1500, 1500 grits) can be placed in the focal plane of L2. This plane is optically conjugated with the sample plane using a 200 mm lens (L3) and a $\times 20$ objective (Mitutoyo Plan Apo SL 20X/0.28). The sample is mounted on a motorized translation stage (PI M-122.2DD1). The sample plane is optically conjugated with an intermediate image plane, using a $\times 20$ objective (Nikon CF Plan 20X/0.35 EPI SLWD) and a 100 mm lens (L4). A second scattering layer composed of two consecutive ground glass diffusers (Thorlabs DG10-600, 600 grits) can be placed in this intermediate image plane. This configuration, with two scattering layers optically conjugated with the sample plane, resembles a situation in which a (moving) sample of interest is located within a (static) disordered material.

Light then passes through a 4f system composed of a 100 mm lens (L5) and 200 mm lens (L6). An iris located in the focal plane in-between the two lenses blocks the light scattered at high angles by the second scattering layer. After passing through a linear polarizer, a 90:10 (transmission:reflection) beamsplitter is used to recombine the reference path with the signal path. The resulting intensity pattern is measured using a complementary metal oxide semiconductor camera (Basler acA1300-200um) with an exposure time of 550 μ s; both quadratures of the complex field are then reconstructed using digital off-axis holography [6]. In order to reduce the influence of unwanted reflections of the reference beam by the camera sensor, all basic optical components have an antireflective coating, and a small angle is introduced between the beam and the normal to the camera.

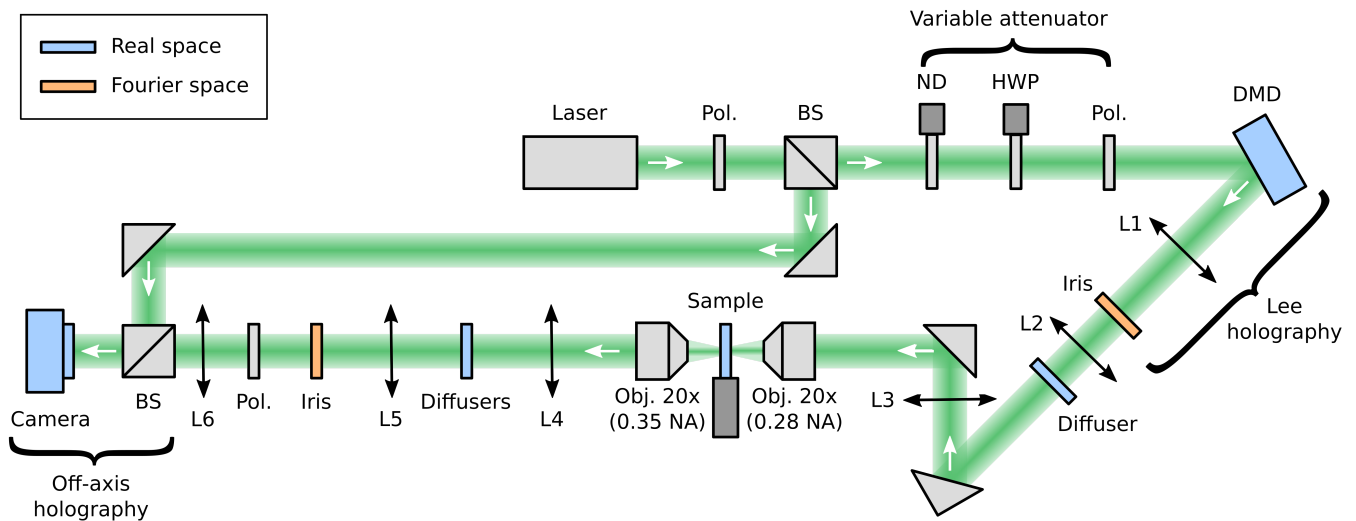


FIG. S2. Schematic of the optical setup used to acquire transmission matrices and perform measurements in low-light conditions. The sample is mounted on a motorized translation stage. The incident field is modulated with a digital micromirror device (DMD) using Lee holography, and the outgoing field is measured by a camera using off-axis holography. Diffusers are placed in intermediate image planes before and after the sample (this configuration optically imitates a situation in which the sample is located within a disordered material). The incident photon flux is controlled with a variable attenuator. Pol, linear polarizer; BS, beamsplitter; ND, neutral density filters; HWP: half wave-plate; Obj, microscope objective; NA, numerical aperture; L1 to L6, lenses.

S3.2. Measured intensity patterns with plane-wave illumination

In order to give a better insight of how complex the system is and how much the beam is spread at the bead location, we use a (clipped) plane wave of normal incidence to illuminate the target without any scattering layer (Fig. S3a), with only the first scattering layer located between the DMD and the sample (Fig. S3b), and with both scattering layers (Fig. S3c). This clearly shows that both scattering layers are complex, since the plane wave becomes a speckle after passing through the first scattering layer, and the speckle is fully different after passing through the second scattering layer. The beam spread induced by the first scattering layer (composed on one single diffuser) is

relatively small; in this way, we can be sure that no more than one bead interacts with the incident field (a few other beads are also located on the same sample, but outside the field of view). In contrast, the beam spread induced by the second scattering later is considerably larger, due to the presence of two contiguous diffusers in-between the sample and the camera.

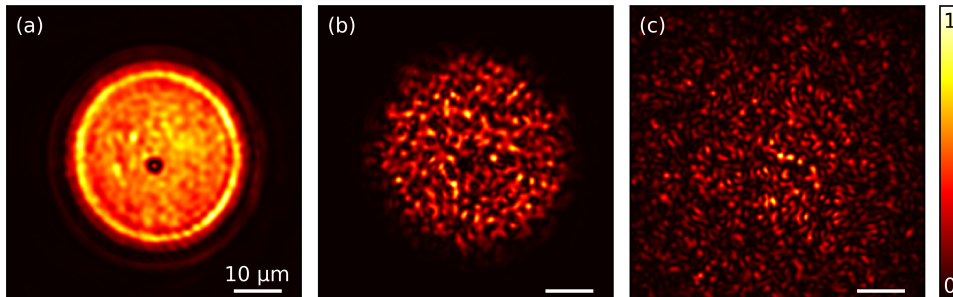


FIG. S3. Intensity distributions measured in the presence of the target for plane wave illumination (a) in the absence of both scattering layers, (b) in the presence of the first scattering layer only and (c) in the presence of both scattering layers.

S4. ACQUISITION PROCEDURE

The acquisition procedure consists of three main steps:

1. We measure transmission matrices with and without the target, with a large number of incident photons. This step allows us to access the discrimination operator D_{12} , from which optimal and average incident states are calculated.
2. We generate the average field state as well as the first 15 eigenstates, with and without the target, and with a large number of incident photons. This step allows us to ensure that the field states predicted from the knowledge of D_{12} can be faithfully generated with our experimental setup. We also perform the same measurements in the absence of the second scattering layer, in order to measure the field distribution in the target plane.
3. We drastically reduce the number of incident photons and we perform a large number of measurements, with and without the target, using the optimal incident state as well as the average one. This step allows us to experimentally quantify the rate of error achievable with each field state as a function of the number of incident photons.

All three steps are performed by running the setup at 1400 Hz, resulting in an effective acquisition rate of 700 Hz. Indeed, for each field that we want to measure, we also acquire a phase-reference field that is generated using a plane wave of normal incidence. This procedure allows us to monitor how the global phase changes over time due to temperature, mechanical and laser wavelength drifts. Global phase drifts are calculated from the complex inner product of all phase-reference fields with the phase-reference field measured at the beginning of the acquisition. Spline interpolations are then used to estimate and correct for the global phase drift at any time during the acquisition. This procedure yields an inter-frame phase error of approximately 0.01 rad.

S4.1. Acquisition of transmission matrices

We measure two (sub-unitary) transmission matrices S_1 and S_2 , relating incident field states to transmitted ones [7]. The matrix S_1 is measured without the target in the field of view, and the matrix S_2 is measured after translating the target inside the field of view. In our experiment, these two transmission matrices are measured in 5.3 s. Note that this time is limited by the acquisition rate of the camera, and could thus be reduced by using a high-speed camera (one could also use a fast single-channel detector since the number of outgoing spatial modes can be taken as low as $N = 1$). Measurements of S_1 and S_2 are performed with no density filter in the signal path, and thus with a large number of incident photons. To illuminate the scattering system, we vary the incidence angle of a plane wave that is clipped to a diameter of 40 μm in the sample plane. More precisely, we sample the incident field in Fourier

space using a triangular lattice [8], covering a numerical aperture of $\text{NA} = 0.25$ with $M = 1735$ different incidence angles. For each angle, we record the transmitted field using digital off-axis holography. This method relies on a reference beam that is tilted by an angle with respect to the signal beam. With this approach, the complex field can be directly accessed in Fourier space by selecting the first-order component. We therefore sample the transmitted field in Fourier space, with the square lattice defined by the pixels of the camera, covering a numerical aperture of $\text{NA} = 0.25$ with $N = 2617$ sampling points. Transmission matrices are therefore measured column by column and, as a result, we obtain 2617×1735 transmission matrices. We normalize these matrices by dividing them by $\sqrt{n_0}$, where n_0 is the number of incident photons associated with each plane wave used to construct the transmission matrices. This number was measured beforehand with a powermeter ($n_0 = 2.2 \times 10^{11}$ photons).

S4.2. Verification of predicted field states

From the knowledge of the two transmission matrices S_1 and S_2 , the discrimination operator $D_{12} = (S_2 - S_1)^\dagger(S_2 - S_1)$ is easily calculated (processing time of 215s). We specifically study the average state, defined as an equally-weighted linear superposition of all eigenstates of D_{12} , as well as the first 15 eigenstates of D_{12} (including the optimal state, which is the first eigenstate of D_{12}). We experimentally generate these states and, for each of them, we perform 50 measurements with and without the target, first in the presence of both scattering layers (in order to compare experimentally-generated light states to predicted ones) and then in the absence of the scattering layer located after the sample (in order to directly measure the field distribution in the target plane).

Averaging over measurements performed in the presence of both scattering layers allows us to compare experimentally-generated light states $|E_i^{\text{out, meas}}\rangle$ to the predicted ones $|E_i^{\text{out, pred}}\rangle = \sqrt{n_0}S_i|\mathcal{E}^{\text{in}}\rangle$. This comparison is achieved by calculating the complex correlation coefficient \mathcal{C}_i and the squared norm ratio R_i , that are respectively expressed by

$$\mathcal{C}_i = \frac{\langle E_i^{\text{out, pred}} | E_i^{\text{out, meas}} \rangle}{\|E_i^{\text{out, pred}}\| \|E_i^{\text{out, meas}}\|}, \quad (\text{S20a})$$

$$R_i = \frac{\|E_i^{\text{out, meas}}\|^2}{\|E_i^{\text{out, pred}}\|^2}. \quad (\text{S20b})$$

Results for the average state and the optimal state are presented in Table S1.

TABLE S1. Fidelity of the experimental generation of light states.

	Single bead		Six beads	
	Average state	Optimal state	Average state	Optimal state
$ \mathcal{C}_1 $	0.97	0.96	0.97	0.96
$ \mathcal{C}_2 $	0.97	0.95	0.97	0.93
R_1	1.3×10^{-1}	5.2×10^{-3}	1.3×10^{-1}	7.2×10^{-3}
R_2	1.3×10^{-1}	5.4×10^{-3}	1.3×10^{-1}	7.4×10^{-3}
η_d	0.98	0.95	0.97	0.91

It clearly appears that the shape of outgoing states is faithfully generated by the DMD, with values of $|\mathcal{C}_i|$ between 0.9 and 1. However, the total intensity experimentally measured is significantly lower than the predicted one, with $R_i \simeq 10^{-1}$ for average states and $R_i \simeq 5 \times 10^{-3}$ for optimal ones. This is explained by the low photon efficiency of techniques based on Lee holography to generate amplitude-and-phase modulated fields [5, 9]: for shaped waves, the actual number of incident photons is equal to $\mathcal{T}_{\text{mod}} n_0$, where \mathcal{T}_{mod} is the fractional transmittance of the modulation technique. Indeed, while phase variations are encoded in the period of a binary grating, amplitude variations are encoded by deflecting photons out of the optical path. The number of incident photons is thus larger for plane waves than for shaped waves. Furthermore, the intensity distribution of optimal states is more spatially localized than those of average states, resulting in a lower photon efficiency of the modulation technique. In practice, the squared norm ratio R_1 can be taken as an estimate of the fractional transmittance \mathcal{T}_{mod} (the choice of R_1 over R_2 is made based on the consideration that values measured in the absence of the target are free of possible positioning errors of the translation stage). Finally, we calculate the ratio η_d between measured and predicted values for d_{12}^2 . We observe that values of η_d are very close to unity, demonstrating that d_{12}^2 is faithfully estimated from transmission matrix measurements.

S4.3. Measurements in low-light conditions

We finally perform many measurements in low-light conditions. To this end, we place a neutral density filter of fractional transmittance $\mathcal{T}_{\text{nd}} = 10^{-3.6}$ in the signal path, and we use the variable attenuator to reduce even more the number of incident photons, with a fractional transmittance \mathcal{T}_{va} evenly varied 6 times between 0.1 and 1. The incident number of photons is thus expressed by $n = \mathcal{T}_{\text{nd}} \mathcal{T}_{\text{va}} \mathcal{T}_{\text{mod}} n_0$. In this way, we vary the number of incident photons from 740,000 to 7,400,000 when the average wave is used, and from 29,000 to 290,000 when the optimal wave is used (the difference between values obtained for the average wave and for the optimal wave is due to different values of \mathcal{T}_{mod}). Since many photons are scattered out of the field of view by the diffusers, only a few photons are actually detected by the camera: the number of detected photons ranges from 14 to 140 when using the average wave, and from 2 to 20 when using the optimal wave. We thus detect on average 1 photon for 53,000 incident photons with the average wave, and 1 photon for 15,000 incident photons with the optimal wave. This demonstrates that the optimal state not only leads to an increased interaction between the light and the object, but also more efficiently redirects the light towards the observer, resulting in a larger ratio between detected and incident photons.

For each value of n , we successively generate the average state and the optimal state and, for each state, we perform $N_{\text{rep}} = 4000$ measurements. As we assume that the *a priori* probabilities for each hypothesis are given by $\pi_1 = \pi_2 = 0.5$, this results in the acquisition of 2000 measurements in the presence of the target and 2000 measurements in the absence of the target. In our experiment, this large data set ($2 \times 6 \times 4000$ measurements) is measured in 104s. We then calculate the log-likelihood ratio for each measured field with Eq. (S18), and we deduce the experimental rate of error based on the decision criterion expressed by Eq. (S17) (processing time of 174s). This is finally compared to the theoretical rate of error expressed by Eq. (S14), where $\sigma^2 = 0.5$ and $d_{12}^2 = \eta_d \langle \mathcal{E}^{\text{in}} | D_{12} | \mathcal{E}^{\text{in}} \rangle$.

S5. INTENSITY DISTRIBUTION OF EIGENSTATES IN THE TARGET PLANE

S5.1. Small target

By performing measurements in the absence of the second scattering layer, we can directly access the intensity distribution of the eigensates of D_{12} in the target plane. The number of significant eigenstates is theoretically determined by the number of modes in the area A_t covered by the target, which can be approximated by $N_t \simeq 2\pi A_t \text{NA}^2 / \lambda^2$ [10]. Using this expression, we obtain a number of modes of the order of 12 for a target composed of a single bead, in agreement with the observed number of eigenvalues that are significantly above the noise floor (see Fig. 2a of the manuscript). It is interesting to study the spatial distribution of the intensity associated with these largest eigenvalues, as such light fields significantly interact with the target.

For a target composed of a single bead (Fig. S4), intensity distributions have a structured aspect that resemble those of Laguerre-Gaussian modes. Assuming that light states are here optimal when they maximize the number of photons

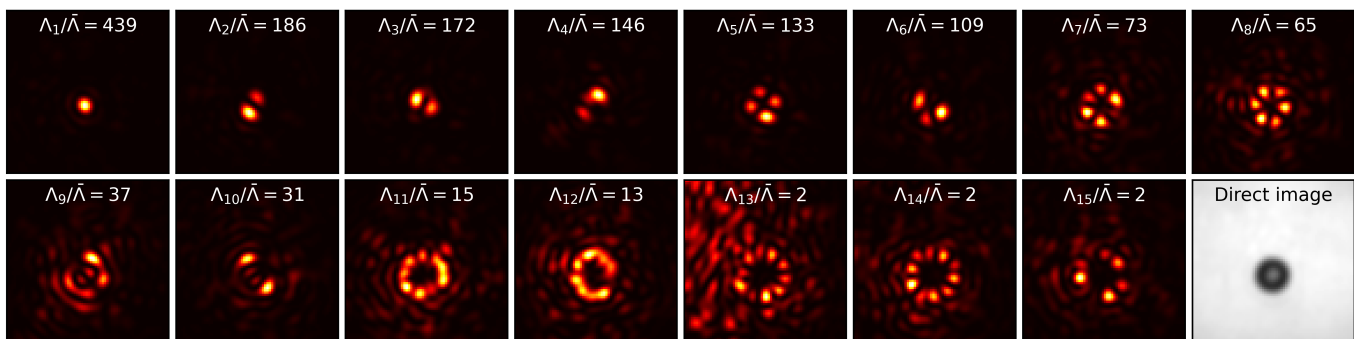


FIG. S4. Intensity distributions measured in the target plane for the first 15 eigenstates of the discrimination operator D_{12} , along with an image of the target measured under spatially-incoherent illumination. The target is here composed of a single bead. All figures correspond to intensity distributions measured in the absence of the target, except for the last figure which is measured in the presence of the target. The field of view (edge size, $19.2 \mu\text{m}$) is centered on the high-intensity area, and color scales are identical to those shown in Fig. 2 of the manuscript.

interacting with the target, these distributions can be understood as arising from a Gram-Schmidt orthogonalization procedure: the first eigenstate generate a strongly focused beam at the target position, and the j -th eigenstate ($j \geq 2$) maximizes the number of interacting photons under the constraint that it must be orthogonal to the $j - 1$ previously-calculated eigenstates. Note that the measured intensity distributions are localized around the target for the 15 eigenstates showed in Fig. S4, and not only for the 12 first eigenstates whose eigenvalues are significantly above the noise level. This suggests that these last eigenstates—associated with eigenvalues Λ_{13} to Λ_{15} —are weakly interacting with the target, at the limit of the detection capabilities of our setup.

S5.2. Extended target

For a target composed of 6 beads (Fig. S5), intensity distributions are all spatially localized around the position of the beads, but the shape of these distributions is more difficult to interpret than for the case of a single bead. For instance, the first eigenstate focuses on 2 beads, while the third eigenstate focuses on 5 beads and the sixth eigenstate focuses on a single bead. These different intensity distributions are likely to be due to the fact that all beads are not equally connected to the far-field modes controlled in the experiment. This clearly shows that, for complex scattering systems, the statistical distance d_{12} cannot be easily maximized by a simple focusing approach.

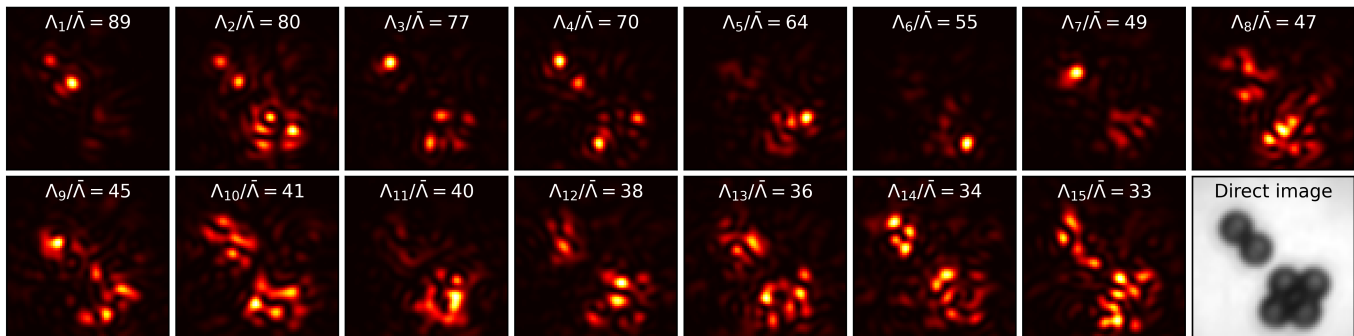


FIG. S5. Analogous to Fig. S4 for a target composed of 6 beads.

-
- [1] R. Loudon, *The Quantum Theory of Light* (Oxford University Press, Oxford, 2000).
 - [2] P. Pai, J. Bosch, M. Kühmayer, S. Rotter, and A. P. Mosk, *Nat. Photonics* **15**, 431 (2021).
 - [3] J. W. Goodman, *Statistical Optics* (John Wiley & Sons, Hoboken, 2015).
 - [4] H. L. V. Trees, K. L. Bell, and Z. Tian, *Detection Estimation and Modulation Theory, Part I* (John Wiley & Sons, Hoboken, 2013).
 - [5] W.-H. Lee, *Appl. Opt.* **13**, 1677 (1974).
 - [6] E. Cuche, P. Marquet, and C. Depeursinge, *Appl. Opt.* **39**, 4070 (2000).
 - [7] S. M. Popoff, G. Lerosey, R. Carminati, M. Fink, A. C. Boccara, and S. Gigan, *Phys. Rev. Lett.* **104**, 100601 (2010).
 - [8] P. Pai, J. Bosch, and A. P. Mosk, *OSA Continuum* **3**, 637 (2020).
 - [9] M. Mirhosseini, O. S. Magaña-Loaiza, C. Chen, B. Rodenburg, M. Malik, and R. W. Boyd, *Opt. Express* **21**, 30196 (2013).
 - [10] A. P. Mosk, A. Lagendijk, G. Lerosey, and M. Fink, *Nat. Photonics* **6**, 283 (2012).